Appl. Phys. A 76, 791–800 (2003)
DOI: 10.1007/s00339-002-1503-8

Applied Physics A
Materials Science & Processing

L. BARBADILLO[1,✉]
M. CERVERA[1]
M.J. HERNÁNDEZ[1]
P. RODRÍGUEZ[1]
J. PIQUERAS[1]
S.I. MOLINA[2]
A. PONCE[2]
F.M. MORALES[2]

$N + BF_2$ and $N + C + BF_2$ high-dose co-implantation in silicon

[1] Laboratorio de Microelectrónica, Facultad de Ciencias, Universidad Autónoma de Madrid, 28 049 Madrid, Spain
[2] Dpto. de Ciencia de los Materiales e Ingeniería Metalúrgica y Química Inorgánica, Universidad de Cádiz, Apdo. 40, Puerto Real, 11 510 Cádiz, Spain

Received: 10 January 2002/Accepted: 30 May 2002
Published online: 4 November 2002 • **© Springer-Verlag 2002**

ABSTRACT Nitrogen and boron BF_2, and nitrogen, carbon, and boron BF_2 high-dose (6×10^{16}–3×10^{17} cm^{-2}) co-implantation were performed at energies of about 21–77 keV. Subsequent high-temperature annealing processes (600, 850, and 1200 °C) lead to the formation of three and two surface layers respectively. The outer layer mainly consists of polycrystalline silicon and some amorphous material and Si_3N_4 inclusions. The inner layer is highly defective crystalline silicon, with some inclusions of Si_3N_4 too. In the N + B-implanted sample the intermediate layer is amorphous. Co-implantation of boron with nitrogen and with nitrogen and carbon prevents the excessive diffusivity of B and leads to a lattice-parameter reduction of 0.7%–1.0%.

PACS 81.05.Je; 81.20.-n; 52.75.Rx

1 Introduction

Cubic boron nitride (c-BN) is probably the second hardest material known after diamond and, like it, it is a good insulator (with a resistivity of 10^{17} Ω cm at room temperature). Additionally, unlike diamond, it has both *p*-type and *n*-type dopants [1], which increases its interest for electronic devices.

According to theoretical work of Liu and Cohen [2–4] the hypothetical compound C_3N_4 would be even harder than boron nitride. This prediction has stimulated much effort in recent years for its synthesis. However, in spite of the great number of publications reporting attempted synthesis of crystalline C_3N_4 with properties close to that of diamond, it appears not to have been achieved so far.

The polytypes of boron nitride have some of the largest band gaps of the III–V nitrides (about 6.4 eV in c-BN and 5.1 eV in h-BN) and are of technological importance for deep-blue and UV optoelectronic applications. There are several reports about unidentified defects and impurity-related deep levels, as well as near-band-gap luminescence from both h- and c-BN (see for instance [5–7]).

✉ Fax: +34-91/3974895; E-mail: Lucia.Barbadillo@uam.es

A large number of physical and chemical vapor deposition (PVD and CVD) techniques have been investigated for the synthesis of c-BN films, including molecular ion beam deposition, ion plating, N_2-ion implantation in boron deposits, radio-frequency reactive sputtering, electron cyclotron resonance, plasma-enhanced CVD, and microwave plasma-enhanced CVD [8–12]. Ion bombardment during thin-film growth has been found to reduce the substrate temperatures needed to prepare good crystalline films.

Given the similarity in the phase diagrams of C and BN, including a hexagonal graphitic stable form at ambient conditions, a high-pressure–temperature hexagonal (würtzite) structure, and a diamond-like (cubic) form, a solid solution should exist across the C–BN system at high pressure.

BCN compounds are expected to have semiconducting properties intermediate between those of metallic graphite and insulating h-BN. They would behave as semiconductors with a 'tunable' band-gap energy, which would be controlled by their atomic compositions and atomic arrangements. Theoretical calculations about graphite-like BC_2N, for instance, give three possible atomic arrangements, two of which have gap energies of a semiconductor [13, 14].

Cubic (β-phase) BCN materials have attracted increasing interest because they may have physical properties similar to diamond and borazon (high strength, good tribological properties, excellent thermal conductivity and resistance to aqueous corrosion, ...) and be, therefore, of potential technological importance. Additionally, c-BCN might overcome some problems of diamond and c-BN (for instance, high internal stresses, which result in a poor adhesion of films on many substrates).

Its mechanical characteristics together with its high optical transparency allow its application in wear protection, as mask substrates for X-ray lithography, low-*Z* layers in pellet targets for laser fusion experiments, composite nanotube heterojunctions, etc. Photoluminescence reports from BC_2N with a peak intensity at wavelengths of 580–600 nm also suggest the possibility of BC_2N-based light-emitting devices [15, 16], for the integration of optoelectronic devices in the silicon technology, and for flat-panel displays. Further, the negative electron affinity of boron nitride allows foreseeing the integration of field-emitter arrays with the silicon technology.

As a new approach, in this paper we report the results of high-dose ion co-implantation of both nitrogen and boron in silicon. We have also added carbon in some of the samples using the same technique, and performed subsequent annealing, as an attempt to synthesize BN and BCN clusters.

2 Experimental

Both-sides-polished (111) n-type float-zone silicon wafers, with phosphorus concentration about $10^{14}\ \mathrm{cm}^{-3}$, were implanted with (i) boron, (ii) nitrogen and boron, and (iii) nitrogen, carbon, and boron in a modified Varian-Extrion ion implanter. The ion-current densities were about $5.6\ \mu\mathrm{A/cm}^2$ for N^+, $3\ \mu\mathrm{A/cm}^2$ for C^+, and between 7.5 and $11\ \mu\mathrm{A/cm}^2$ for BF_2^+. Implantation conditions (doses and energies) are summarized in Table 1. Energies were selected to obtain a projected range of about 650 Å in all cases, as predicted by the SRIM program [17]. Doses were chosen to obtain a peak concentration of the implanted ions similar to the bulk silicon density, $5\times10^{22}\ \mathrm{cm}^{-3}$. All of them were well over the threshold amorphization dose.

During the process, with the ion-current densities used, the mean temperature increase induced by the beam in the sample holder should not have exceeded 150 °C. Nevertheless, the sample holder was maintained cool by a closed-cycle cooling system. Afterwards, the implanted samples were annealed in pure nitrogen atmosphere to recrystallize the Si overlayer and to promote the activation and/or chemical reaction of the implanted ions. The annealing processes were carried out for one minute in rapid thermal annealing (RTA), at 600, 850, and 1200 °C, and for three hours in a conventional furnace also at 1200 °C.

Fourier transform infrared (FTIR) spectra in transmission mode were collected with a Bruker IFS-66 V spectrometer. This technique was used to identify the vibrational modes of the different bonds present in all the samples and, thus, to follow the reaction between the implanted ions and the silicon matrix.

High-resolution X-ray diffraction (HRXRD) measurements were performed in a Siemens D-5000 diffractometer, using the Cu K_α radiation at 1.54 Å as the source for diffraction. These results allowed us to check the crystalline quality of the Si overlayer of the implanted samples annealed at higher temperatures, both in RTA and a conventional furnace.

Spreading resistance (SR) measurements were used to test the surface-layer resistivity changes and to estimate the impurities' distribution.

The structural changes originated in silicon by ion implantation have been studied by conventional transmission electron microscopy (TEM), high-resolution electron microscopy (HREM), and selected-area electron diffraction (SAED). Conventional TEM work was carried out in a Jeol 1200 EX while a Jeol 2000 EX was operated for HREM studies. SAED analysis was performed using both transmission electron microscopes. Electron-diffraction patterns and HREM image analysis were carried out using Digital Micrograph and Semper software. All studies were carried out after preparing cross-section (X) specimens by mechanical thinning and further Ar^+-ion milling at 4.5 kV.

Spectroscopic ellipsometry (SE) measurements of the samples were performed in a Uvisel Jobin–Yvon spectrometer between 1.5 and 4.5 eV. The SE measurements were fitted to adequate models to deduce the layer structure and thickness.

Implanted elements	Implantation energy (keV)	Dose (cm^{-2})
N	25	6×10^{16}, 3×10^{17}
C	21	3×10^{17}
BF_2 (B)	77	6×10^{16}, 3×10^{17}

TABLE 1 Implantation conditions

3 Experimental results

3.1 *FTIR results*

FTIR measurements were performed in all the samples. An unimplanted silicon wafer is used as a reference, but no baseline corrections have been done. Figure 1 shows the spectra of the samples implanted with $N^+ + B^+$ (Fig. 1a) and $N^+ + C^+ + B^+$ (Fig. 1b), before and after RTA processes. The spectra of the samples implanted just with boron are not shown because the only important result is the remarkable bending/bowing that the baseline displays after high-temperature annealing of the samples. This bending is also present in the other samples (see Fig. 1). It is due to the activation of the implanted boron, which produces a strong increase of the free-carrier absorption, and increases as the growing annealing temperature activates the implanted boron ions electrically. In some cases this bowing can almost mask some broad bands.

In some spectra the measured transmittance apparently takes values higher than 1. This effect is due to the anti-reflecting behavior of the external layer in the implanted samples, which leads to an overestimation of the sample transmittance.

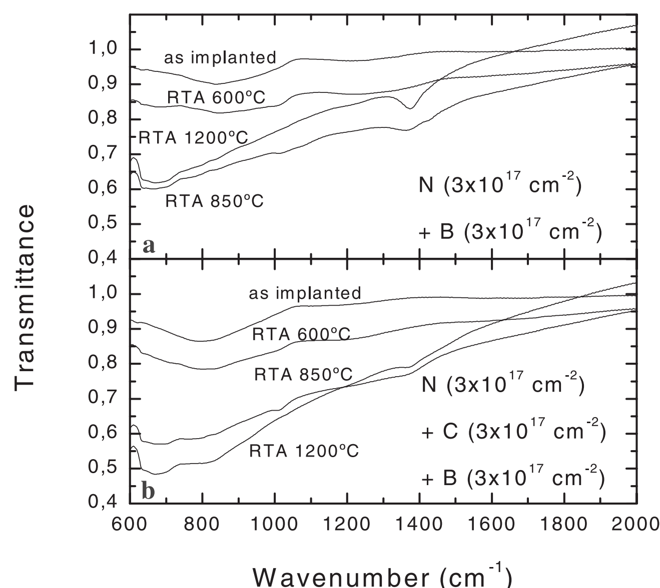

FIGURE 1 FTIR spectra of the samples implanted with **a** nitrogen and boron, and **b** nitrogen, carbon, and boron, before and after RTA annealing

The FTIR spectra measured in the samples before annealing and after the 600 °C process display two main bands. Both are extremely broad (FWHM $\geq 200\,cm^{-1}$), because after low-temperature annealing the structural damage and bond-angle distortions caused by the implantation over the solubility limit still remain. The first one is located at about 800–900 cm^{-1} and is due to the vibrational modes of Si–C and/or Si–N bonds, which are usually placed at about 780 cm^{-1} and 850 cm^{-1} respectively [18, 19]. The second one is a broad absorption band at about 1300 cm^{-1}, which is more visible in the higher-dose-implanted samples. As the annealing temperature increases, this peak becomes progressively narrower, peaking at 1375 cm^{-1}, which is usually associated with the stretching band of sp^2-bonded BN (in amorphous or crystalline hexagonal arrangement) [20].

As the samples are subjected to higher-temperature annealing the first broad band seems to decrease (or, at least, to be masked by the free-carrier absorption). This decrease may be explained by a trend of nitrogen to bond with boron atoms.

As the Si–N band almost disappears with the high-temperature annealing, a peak at about 1020 cm^{-1} becomes visible in all spectra, even in the one from the sample implanted only with boron. We identify it as the Si–O stretching band from the surface native oxide, which is usually located at about 1080 cm^{-1} [18], but that can be shifted towards lower wavenumbers because of a softening of the bonds due to the presence of boron in the native oxide.

This region of some spectra is shown in Fig. 2. A local baseline has been taken in each of them to have a clear presentation. In most of them only the contribution at about 1020 cm^{-1} attributed to surface oxidation can be seen. Nevertheless, in the sample implanted with $3\times10^{17}\,cm^{-2}$ of nitrogen and boron and annealed at 850 °C, a second contribution can be distinguished at about 1075 cm^{-1}. Since we consider that the Si–O stretching due to surface oxide is the first one, we cannot disregard the possibility of the second being caused by some B–N bonds in a cubic arrangement (whose stretching band is usually located at about 1075 cm^{-1}) [21].

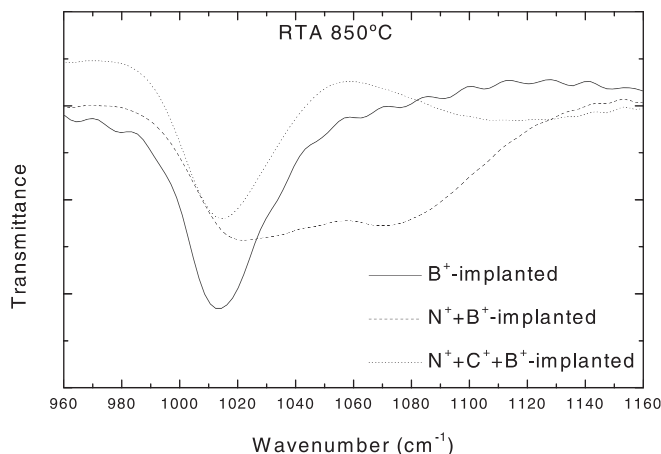

FIGURE 2 Zoom of the region around 1050 cm^{-1} of the FTIR spectra of the samples implanted with a dose of $3\times10^{17}\,cm^{-2}$ of each ion, and annealed at 850 °C for 1 min

In the $N+C+B$-implanted sample this band at about 1080 cm^{-1} cannot be seen. It suggests that the carbon presence must have prevented the formation of c-BN structures.

Otherwise, the FTIR spectra of the samples implanted also with carbon are very similar to those with nitrogen and boron. The only exception is the additional broadening in the Si–N band that we mentioned before and that is caused by the contribution of the Si–C bond stretching band, usually located at about 780 cm^{-1} [15].

The spectra of the samples annealed for three hours at 1200 °C (conventional furnace) are not shown because the bowing due to free-carrier absorption is so strong that we cannot distinguish clearly the position, or even the presence, of these bands. Probably, boron location in substitutional positions causes the increase of free carriers and its diffusion causes a decrease in the number of B–N bonds.

No traces of C–N or B–C bonds have been observed in the IR spectra of any of the samples. However, the presence of the broad band at 1300 cm^{-1} could have masked them.

3.2 *XRD results*

The surface of the silicon wafers employed as substrates becomes completely amorphous after implantation at such high doses. In order to recover the surface crystallinity, the samples were annealed at growing temperatures. Since all the implanted doses are over the silicon amorphization threshold for these ions, the annealing processes would allow activating a fraction of the implanted impurities, as the amorphizated layer recrystallizes. XRD measurements have been carried out to check this recovery and to learn of possible structural effects of the implantation and annealing processes. Figures 3, 4, and 5 show the rocking curves of the samples implanted with $3\times10^{17}\,cm^{-2}$ of B^+, N^++B^+, and $N^++C^++B^+$ and annealed at 1200 °C for 1 min (RTA) and 3 h (furnace). The rocking curves showed broad bases in all cases, but narrow Si-(111) peaks in those samples implanted with high doses and several species. It may indicate that the surface layer of the substrate remains polycrystalline, although highly ordered after the annealing processes. In the boron-implanted samples, see Fig. 3, the (111) silicon peak looks extremely broadened, indicating that, even after the 1200 °C annealing, the structural order of the silicon lattice remains damaged by the high-dose implantation. The FWHM of the peak in the RTA and furnace-annealed samples is about three and six times larger than in an unimplanted silicon reference, respectively. However, the co-implantation of nitrogen apparently helps to recover the structural order. In Fig. 4 the rocking curves of the samples implanted with $3\times10^{17}\,cm^{-2}$ of nitrogen and boron and annealed at the highest temperatures are displayed. The (111) peak is extremely narrow, especially after the 3 h furnace annealing, meaning a crystalline quality clearly better than in the sample implanted only with B^+, with a value of the FWHM similar to that of the silicon reference. In the samples implanted also with carbon (see Fig. 5) the crystalline quality is as high as in the $N+B$-implanted samples.

All samples show a weak secondary contribution on the right-hand side of the (111) substrate peak, about 0.1° away from it. Since it is present in all cases, it must be an ef-

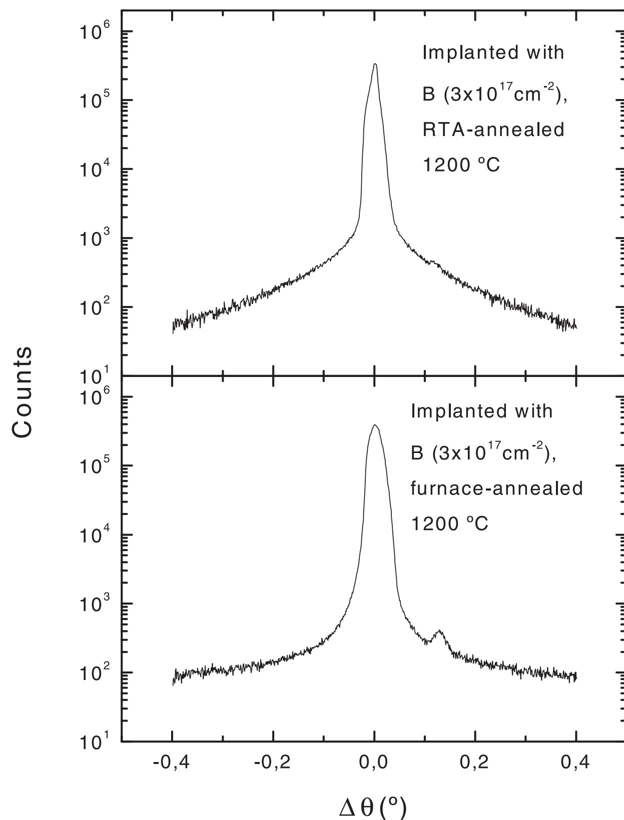

FIGURE 3 XRD rocking curves of the samples implanted with a dose of 3×10^{17} cm^{-2} of boron, and annealed at 1200 °C for 1 min and 3 h

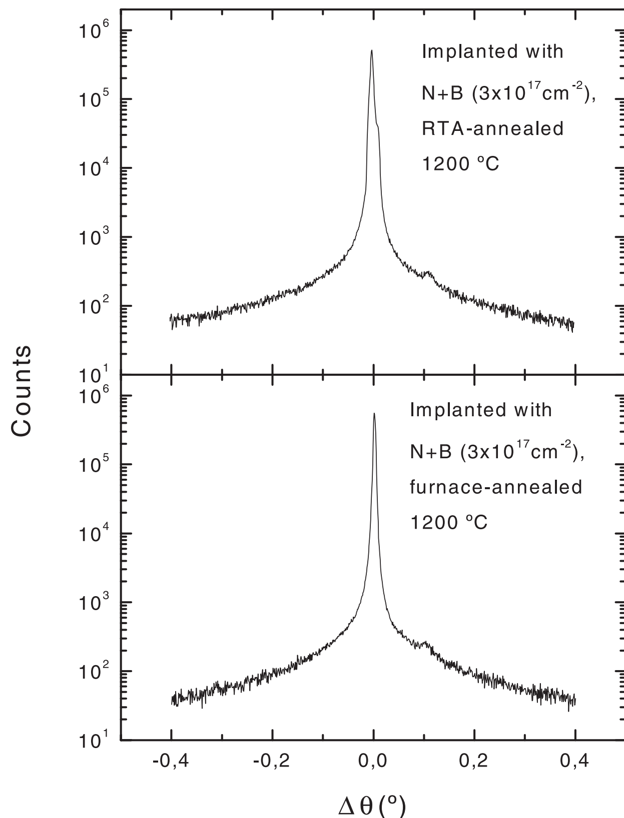

FIGURE 4 XRD rocking curves of the samples implanted with a dose of 3×10^{17} cm^{-2} of nitrogen and boron, and annealed at 1200 °C for 1 min and 3 h

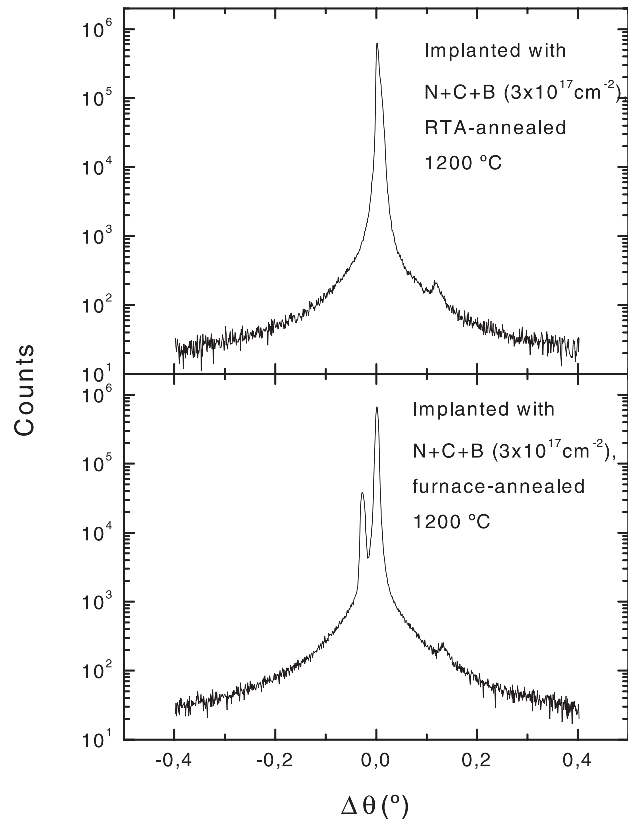

FIGURE 5 XRD rocking curves of the samples implanted with a dose of 3×10^{17} cm^{-2} of nitrogen, carbon, and boron, and annealed at 1200 °C for 1 min and 3 h

fect of the boron implantation, the only one that has been performed in all the samples. The incorporation of nitrogen or carbon in substitutional sites may be reduced due to two causes: formation of Si_3N_4 or SiC structures, and competition of boron atoms. These are expected to occupy lattice positions preferentially during recrystallization because of their covalent radii (0.82 Å in B and 0.75 Å in N, versus 1.02 Å in Si). The same will happen in the case of carbon implantation, whose covalent radio is 0.77 Å. Substitutional incorporation of boron atoms to the silicon lattice, just up to the solubility limit, will cause an effective reduction of the lattice constant of about 0.82%. In practice, it seems to cause a reduction of the lattice parameter in all samples of about 0.7%–1.0%, depending on the ions co-implanted and the annealing processes carried out. The results of this reduction are shown in Table 2. The increase in the width of the main silicon peak and in the impurity-induced lattice contraction present the same annealing behavior.

In the samples implanted just with boron, this reduction is about 0.76% after RTA, while it is stronger (0.87%) after furnace annealing because the longer annealing and, thus, deeper diffusion, enhances a higher incorporation of implanted ions in lattice sites. A decrease in the number of interstitials, which compensate the effect of substitutional atoms in the contraction of the lattice, would also be a possible explanation.

This also happens in the one implanted with the lower doses of nitrogen and boron (6×10^{16} cm^{-2} each). In this case the reduction is about 0.81% after RTA, and 1% (0.19% stronger) after the furnace annealing. Diffusion promotes the

Implanted species	Dose (cm^{-2})	1200 °C RTA samples		1200 °C furnace-annealed samples	
		Δa (%)	FWHM	Δa (%)	FWHM
B^+	3×10^{17}	0.76%	0.010°	0.87%	0.020°
$N^+ + B^+$	6×10^{16}	0.81%	0.00750°	1.00%	0.00810°
	3×10^{17}	0.77%	0.00580°	0.70%	0.00410°
$N^+ + C^+ + B^+$	3×10^{17}	0.80%	0.00450°	0.87%	0.00550°

TABLE 2 Reduction of the silicon lattice constant and FWHM of the main (111)-silicon peak after ion implantation depending on the implanted species and the annealing processes performed

incorporation of B and N atoms in the lattice (or their decrease in interstitial sites), and thus the reduction is stronger.

From Figs. 4 and 5 we deduce that the presence of additional ions (nitrogen and/or carbon) enhances the recrystallization process. This can be due to a 'gettering' effect in Si_3N_4 microcrystals, which probably helps to eliminate the boron excess, forming boron nitride clusters. FTIR spectra are in good agreement with this hypothesis.

In the sample implanted with the higher dose of nitrogen and boron (3×10^{17} cm^{-2} each), the reduction of the lattice constant is stronger after RTA than after the longer annealing (about 0.77 and 0.70% respectively), oppositely to what happened in the sample implanted just with boron. A possible explanation for this phenomenon is that this longer annealing (3 h causes many of the B and N implanted atoms to react and segregate out of the silicon lattice, forming BN clusters. Thus, the number of substitutionals left is lower than after the RTA and the reduction of the lattice constant is also lower. Additionally, diffusion effects may be attenuated by a higher density of Si_3N_4 nuclei, which produce the 'gettering' effect of B mentioned above.

Although after the introduction of carbon (sample implanted with 3×10^{17} cm^{-2} of nitrogen, carbon, and boron) this effect must also be important, the presence of high concentrations of carbon apparently causes an additional contraction. A possible explanation may be the additional incorporation of carbon atoms in substitutional sites. In this case the trend is again the same as in the first cases, with a reduction in the lattice parameter of about 0.87% after furnace annealing, 0.07% stronger than after RTA (0.80%).

In this last sample, co-implanted with the three ions, another secondary peak, much stronger than the one due to lattice reduction, appears on the left of the main one. Although the formation of a new and unknown crystalline phase cannot be completely disregarded, this may indicate the separation of the surface layer into two regions: one in contraction, whereas the other is in expansion. After RTA the surface region may rest in a metastable state, and longer annealing leads to a segregation of carbon atoms. These carbon atoms may occupy interstitial sites in part of the surface region, causing lattice expansion. This effect has been previously observed in silicon implanted with carbon well above its solubility limit. After low-temperature annealing, most of the carbon atoms occupy interstitial sites, causing lattice expansion, while higher-temperature annealing leads to SiC cluster formation. Since the Si–C bond has a lower size than the Si–Si one, the SiC formation enables the relaxation of the lattice and the crystallinity recovery [22]. In the underlying region excess carbon or SiC clusters may act as diffusion sources, inducing an additional lattice contraction in the furnace-annealed sample.

3.3 *Spreading resistance measurements*

The spreading resistance results have allowed us to estimate the depth reached by the implanted ions after diffusion processes caused by thermal annealing. In Fig. 6 we see that boron ions, implanted at a projected range of 650 Å, reached a depth of about 0.7 μm after the 1200 °C RTA process, as the compensation effect shows. Nitrogen and boron co-implantation helps the recovery of the structural order and thus the diffusion of boron, as compared to the B-implanted sample. In Fig. 6b we see that the boron reaches a depth of 0.85 μm in this case. Carbon implantation, oppositely, seems to retain/hold boron, lowering the diffusion coefficient. The cause of this effect may be that the presence of carbon prevents the so-called transient enhanced diffusion (TED) of dopants such as boron in silicon, as suggested by some authors [23, 24].

After furnace annealing (results shown in Fig. 7), boron ions, when no other species are implanted, reach 4.2 μm of

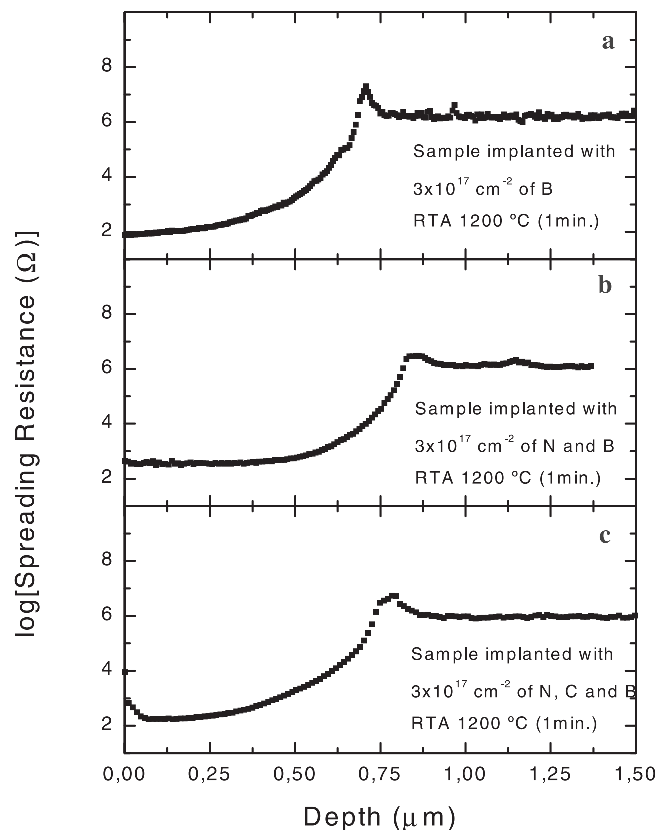

FIGURE 6 Spreading resistance measurements of the samples implanted with 3×10^{17} cm^{-2} of **a** boron, **b** nitrogen and boron, and **c** nitrogen, carbon and boron and annealed at 1200 °C for 1 min

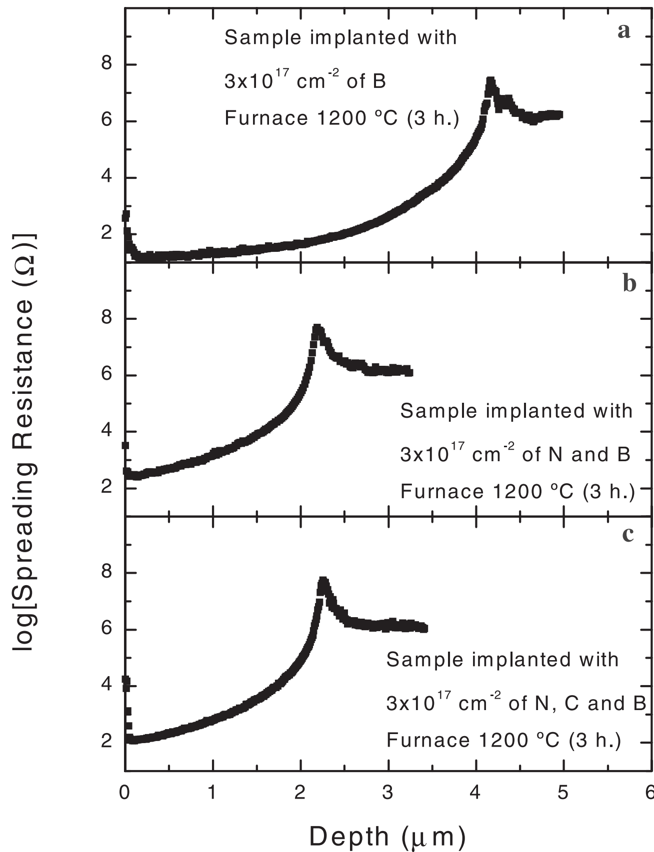

FIGURE 7 Spreading resistance measurements of the samples implanted with 3×10^{17} cm^{-2} of B/N+B/N+C+B and annealed at 1200 °C for 3 h

depth, but in both N + B and N + C + B-co-implanted samples there is an apparent decrease in the diffusion coefficient. This difference with RTA-annealed samples may be due, again, to an effect of reduction of the transient enhanced diffusion of boron due to the presence of the co-implanted impurities. These must, somehow, fix silicon self-interstitials and, reducing the silicon interstitial flux, reduce *interstitialcy* driven processes, such as boron diffusion. The formation of B–N bonds would also retain boron diffusion.

3.4 *Transmission electron microscopy*

XTEM images of Fig. 8a and b correspond to samples implanted with $N^+ + B^+$ annealed (a) for one minute in RTA at 1200 °C and (b) for three hours at 1200 °C, respectively. As a result of the implantation and annealing processes three layers (1, 2, and 3 in Fig. 8a and b) were formed in both samples. The thickness of each layer, measured from XTEM images, is shown in Table 3. SAED and HREM analysis of the three layers formed in these samples demonstrate that, for both samples, layers 1 and 3 are crystalline layers constituted mainly by Si crystals. On the contrary, layer 2 is found to be amorphous.

Figure 9 shows a SAED pattern registered from the three formed layers in the sample implanted with $B^+ + N^+$ and annealed at 1200 °C for 3 h. The electron beam was kept along [110] of the Si substrate. Analysis of additional SAED registered from each layer allows the spot assignation of SAED

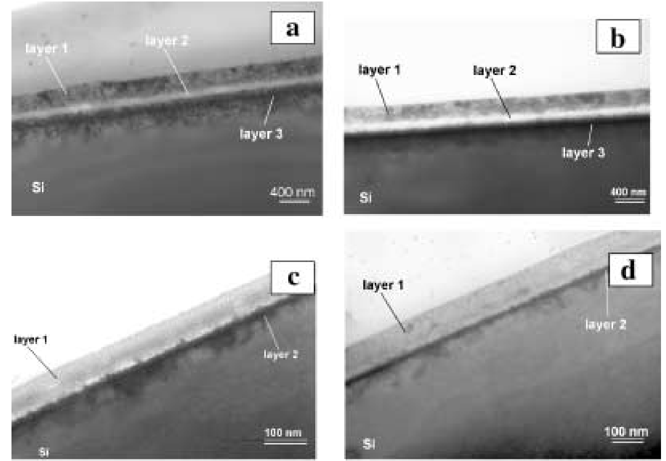

FIGURE 8 XTEM images of samples implanted with $N^+ + B^+$ annealed (at 1200 °C): **a** in RTA for 1 min, **b** for 3 h; with $N^+ + B^+ + C^+$ annealed (at 1200 °C): **c** in RTA for 1 min, **d** for 3 h

Sample	Layer thickness measured by XTEM		
	Layer 1 (Å)	Layer 2 (Å)	Layer 3 (Å)
Si (BN) RTA	1650±100	750±50	1700±100
Si (BN) 3 h	1600±50	850±50	1050±100
Si (BCN) RTA	840±60	450±150	–
Si (BCN) 3 h	960±60	250±60	–

TABLE 3 Thickness of the layers detected in the samples implanted with nitrogen and boron and with nitrogen, carbon, and boron, after 1200 °C annealing processes of 1 min (RTA) and 3 h (conventional furnace)

of Fig. 9 as follows. Spots encircled are due to monocrystalline Si from layer 3, while spots marked with squares are due to microtwins existing in this layer. The rings are indexed assuming that layer 1 is constituted for polycrystalline Si. Though the majority of the crystals in layer 1 are formed by Si, some few spots assigned to α-Si_3N_4 and β-Si_3N_4 are found in the SAED patterns registered from this layer. This means that layer 1 consists of a polycrystalline Si matrix with crystalline inclusions of α-Si_3N_4 and β-Si_3N_4. Spots X_1

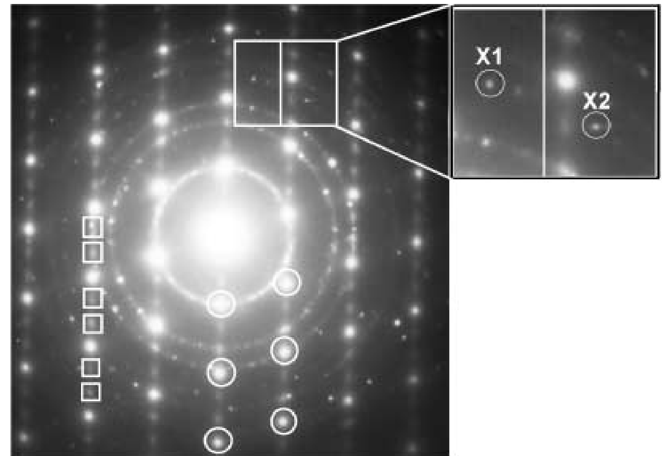

FIGURE 9 SAED pattern of sample implanted with $N^+ + B^+$ annealed at 1200 °C for 3 h. Spots have been marked with *circles* (Si matrix and layer 3) and *squares* (microtwins in layer 3). The amplified image on the *right-hand side* shows spots X_1 and X_2 assigned to α-Si_3N_4 and β-Si_3N_4, respectively

and X_2 of the amplified SAED pattern on the right-hand side of Fig. 9 are assigned to α-Si_3N_4 and β-Si_3N_4, respectively. The lattice spacing measured for X_1 is 0.1310 ± 0.0016 nm and it is assigned to the lattice spacing of 0.1322 nm [associated with planes (−1 −3 3), (−1 4 3), (3 1 3), (4 −3 3), (3 −4 3), (−3 −1 3), (−3 4 3), (−4 1 3), (4 −1 3), (−4 3 3), or (1 −4 3) of α-Si_3N_4]. The measured lattice spacing for spot X_2 is 0.1367 ± 0.0010 nm and it is assigned to the lattice spacing of 0.1359 ± nm [associated with planes (–1 –1 2), (–1 2 2), (–2 1 2), (2 –1 2), (1 –2 2), or (1 1 2) of β-Si_3N_4]. An analogous SAED study of layer 1 in the sample annealed in RTA demonstrates the existence of crystalline inclusions of α-Si_3N_4, though β-Si_3N_4 was not detected.

Figure 8c and d show that two thin layer contrasts are visible in XTEM images of samples implanted with N^+, B^+, and C^+. The thickness of layers 1 and 2 (see Table 3) do not suffer strong changes after the annealing for 3 h at 1200 °C. A HREM study of layer 1 shows, both for the sample annealed in RTA for one minute and the sample annealed for 3 h, that this layer consists of polycrystalline Si mixed with amorphous material. However, the annealing for 3 h causes a strong decrease of the percentage of amorphous material in layer 1. Figure 10a and b present HREM images of layer 1 of samples implanted with N^+, B^+, and C^+ annealed in RTA for one minute and for 3 h, respectively. From these images there is evident the crystallinity increase produced by the annealing for 3 h. The encircled region of Fig. 10a corresponds to a Si nanocrystal in the amorphous matrix. Such nanocrystals are found to be dispersed in layer 1 in the samples annealed in RTA for one minute. Layer 2 consists of monocrystalline Si with many planar defects. Figure 10c presents a HREM image of a zone of layer 2 rich in planar defects.

By SAED pattern analysis, crystalline inclusions have also been determined to be present in the matrix material of layer 1 in samples implanted with N^+, B^+, and C^+. The presence of α-Si_3N_4 can be confirmed from SAED analysis for both samples (annealed with RTA for one minute and for 3 h). Figure 11 shows a SAED pattern registered from a sample annealed for 3 h where two spots (Y_1 and Y_2) do not correspond to Si. The measure lattices spacing for spots Y_1 and Y_2 are 0.2252 ± 0.0018 nm and 0.2670 ± 0.0024 nm, respectively. If we assume possible binary compounds formed combining Si, C, B, and N, spot Y_1 only can be assigned to β-C_3N_4 (lattice spacing of 0.2250 nm). On the contrary, spot Y_2 can be assigned to several crystalline phases: β-Si_3N_4 (lattice spacing of 0.2663 nm), 2H−SiC (lattice spacing of 0.2664 nm), 4H−SiC (lattice spacing of 0.2668 nm), and 8H−SiC (lattice spacing of 0.2606 nm). Crystalline inclusions of β-C_3N_4 are only detected in the sample annealed for 3 h, and this phase is not found in the sample annealed in RTA for one minute. However, as the SAED pattern of Fig. 11 shows, the presence of other crystalline phases cannot be discarded in the sample annealed for 3 h.

3.5 *Spectroscopic ellipsometry*

Spectroscopic ellipsometry measurements were performed between 1.5 and 4.5 eV using a Uvisel Jobin–Yvon

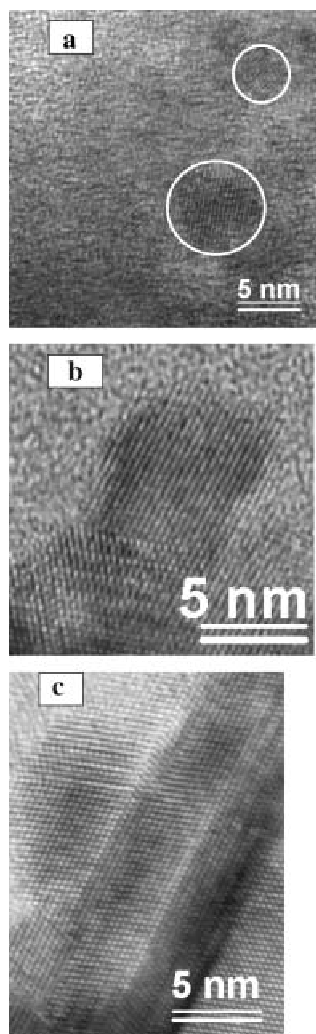

FIGURE 10 HREM images of samples implanted with $N^+ + B^+ + C^+$ annealed at 1200 °C (**b**, **c**) and in RTA for 1 min (**a**) registered from layers 1 (**a** and **b**) and 2 (**c**)

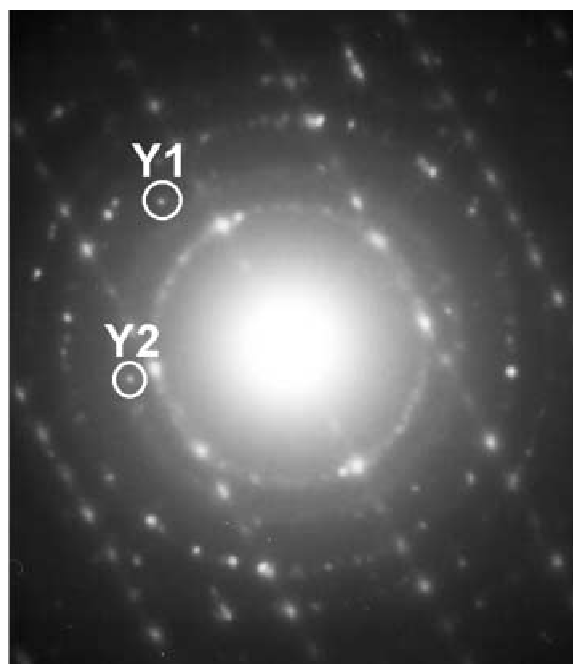

FIGURE 11 HREM images of samples implanted with $N^+ + B^+ + C^+$ annealed at 1200 °C for 3 h. Spots Y_1 and Y_2 correspond to crystalline inclusions in layer 1

ellipsometer, with an experimental accuracy in the ellipsometric angles, ψ and Δ, better than 0.02°.

It is possible to estimate the composition and the thickness of the resulting films by means of a conventional procedure [25]. It is based on a least-squares fitting done by fixing initial values and varying them to minimize the sum of the errors in the equations that relate the measured ellipsometric angles ψ and Δ and the optical properties of the films (refractive indexes and absorption coefficients) [26, 27].

Using different theoretical approaches of the effective medium to simulate the optical properties of the films by changing the relative concentration of its components, this technique can be applied to the analysis of inhomogeneous films. In our case we have used only the two main approximations. The Maxwell–Garnett model (see for example [25, 28]) is employed when the main component (a) can be considered as a 'host' (h) for the others (over 75% in composition), and thus the dielectric constant of this main component is considered as the dielectric constant of a 'host' in which the other components are included ($\varepsilon_h \approx \varepsilon_a$). The Bruggeman model [25, 28] is applied when components ($a, b, \ldots$) are in similar proportions and allows us to obtain the effective dielectric constant by considering as 'host' the effective medium itself ($\varepsilon_h = \varepsilon$).

The sensitivity of the technique is limited to the outer few thousands of angstroms, since the absorption constant, α, of silicon is between 10^3 and 10^5 cm^{-1} in the spectral range of measurements. In fact the fittings have been done taking into account only the first 650–1300 Å. This means that, in all cases, we are seeing just a part of the outer layer observed in TEM analysis, in which only polycrystalline silicon and some inclusions of Si_3N_4 were detected. Thus, other components (boron nitride, silicon carbide, etc.) that are detected by SE should be in amorphous form in this region or, if crystalline, in very low concentrations. Oppositely, crystalline inclusions of Si_3N_4 have been detected by TEM and not by SE; this may indicate that it is present only in small concentrations and, being almost transparent for ellipsometry, it cannot be clearly distinguished from BN contributions.

Figures 12 and 13 show the spectra of the pseudodielectric constant of the samples implanted with nitrogen and boron, and nitrogen, carbon, and boron, respectively, and their fittings.

In the sample implanted only with N + B, RT-annealed (Fig. 12a) no reasonable fitting could be obtained, but any of the best trials included the presence of amorphous silicon (a-Si) and hexagonal boron nitride (h-BN) as the most abundant species just below a thin surface layer of native silicon oxide (SiO_2).

In these fittings h-BN can mean amorphous (a-BN) or crystalline hexagonal boron nitride, formed by B–N sp^2 bonds, as has been mentioned. This explains why it has not been detected by SAED. It can be forming an amorphous matrix in which just minor crystalline inclusions (as silicon nitride) would be seen by SAED results.

The pseudodielectric constant of the N + C + B-implanted layer, RT-annealed (Fig. 13a) has a slight similarity to the dielectric constant of h-BN, although with an effective gap en-

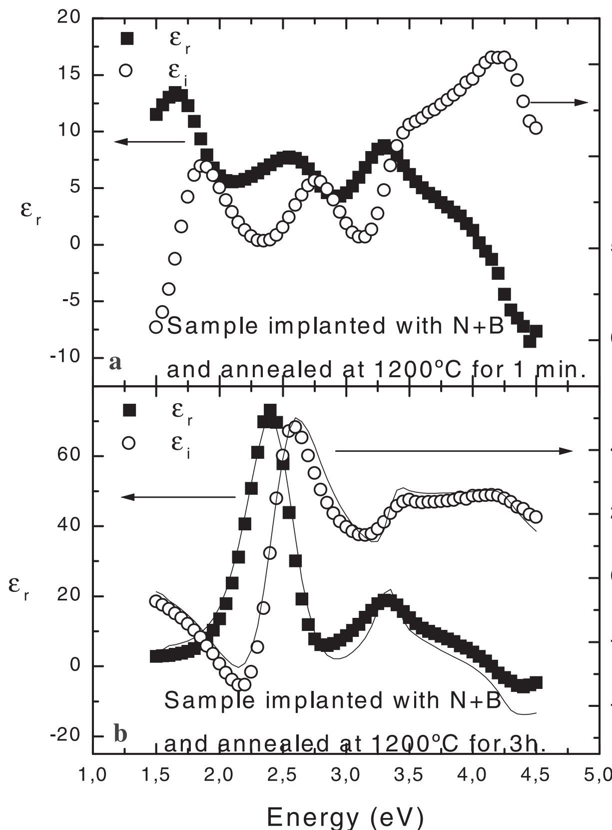

FIGURE 12 Ellipsometry measurements of the samples implanted with N^+ and B^+ (3×10^{17} cm^{-2} each), annealed at 1200 °C for 1 min (**a**) and 3 h (**b**)

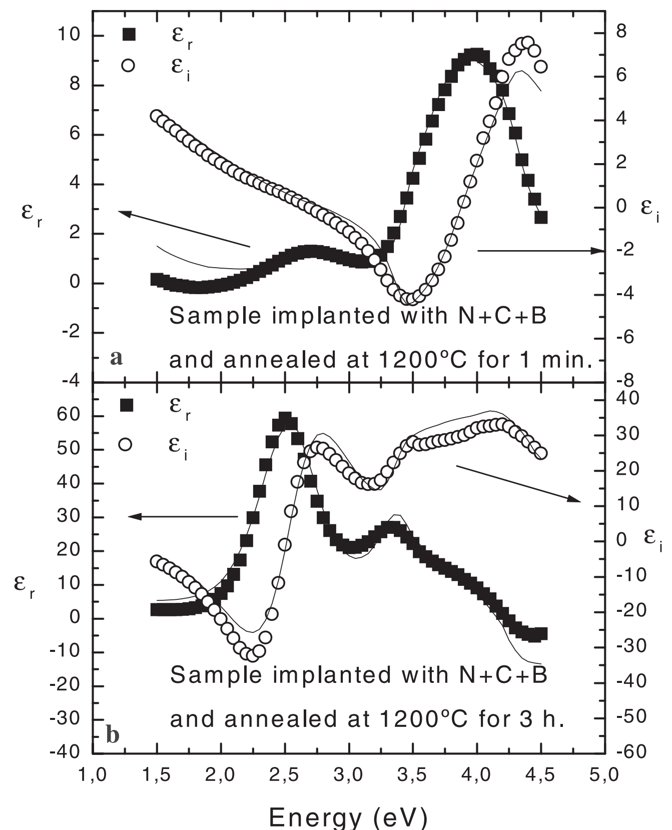

FIGURE 13 Ellipsometry measurements of the samples implanted with N^+, C^+, and B^+ (3×10^{17} cm^{-2} each), annealed at 1200 °C for 1 min (**a**) and 3 h (**b**)

	Layer 1	Layer 2	Layer 3
Sample implanted with N + B, annealed for 3 h	322 Å of {51% c-Si+26% a-Si+23% SiB21}	–	372 Å of {72% h-BN+21% a-Si+7% SiB21}
Sample implanted with N + C + B, annealed for 1 min	130 Å of {84% h-BN+16% voids}	127 Å of {84% h-BN+16% a-Si}	368 Å of {67% h-BN+19% a-Si+14% SiC}
Sample implanted with N + C + B, annealed for 3 h	156 Å of {53% SiB21+39% a-Si+8% c-Si}	280 Å of {45% SiC+33% c-Si+22% a-Si}	263 Å of {77% h-BN+14% SiB21+9% a-Si}

TABLE 4 Composition of the outer layers of the samples, according to SE fittings. (Layer 1 corresponds to the most external layer and layer 3 to the deepest of them)

ergy of around 3 eV, well below that of h-BN (about 5.1 eV, see [29]). The best fit corresponds to an external layer consisting mostly of h-BN with some porosity near the surface (simulated with 'voids') and some inclusions of a-Si and even some silicon carbide (SiC) in the inner part of the layer. To simulate the varying composition, the layer structure has been divided into three sub-layers as quoted in Table 4.

The experimental pseudodielectric constants of the samples implanted with N + B and N + C + B and annealed at 1200 °C for 3 h (see Figs. 12b and 13b) look very similar. In any of the two samples crystalline silicon after implantation has been simulated as a mixture of pure silicon (c-Si), with data from Aspnes and Theeten [26], and heavily doped-with-boron silicon (10^{21} cm^{-3}), using data taken from measurements of Viña and Cardona [30], 'SiB21' in our table.

In both samples, the composition of the most external layer has a strong effect on the quality of the fittings, but significant changes in the fractions of the different species included in the inner layers lead to equally reasonable fittings. In both cases, the most external layer consists mostly of crystalline silicon (mixture of c-Si + SiB21) and a-Si. Both fittings require a significant fraction of h-BN in the inner layer. The only difference between the fittings is the requirement of an intermediate layer with an appreciable content of SiC in the N + C + B-implanted sample.

After the 3-h 1200 °C annealing, it was not necessary to include any BN in the external layers. Probably, boron nitride decomposes at such high temperatures, and both B and N out-diffuse and evaporate from the surface after prolonged treatments.

4 Discussion

As the annealing temperature increases, both samples co-implanted with N + B and with N + C + B show a trend to separation into Si_3N_4, h-BN, or a-BN phases, and SiC in the last case, as evidenced by FTIR results. However, FTIR spectra offer only overall and qualitative information of the composition in the surface regions. A closer view may be obtained by considering the results of the other techniques. However, we have to have in mind that each of them offers information about different regions of the samples. Only the near-surface layers have been analyzed by TEM, HREM, and SAED. On the other hand, spreading resistance measurements show the behavior of the diffusion in the underlying regions, where impurities are of the order of or below the solubility limit, and thus electrically activated. On the contrary, ellipsometry is sensitive only to a part of the most external layer seen by TEM (layer 1). Finally, XRD gives information only of crystalline or highly ordered layers.

The annealing behavior of the B-only-implanted sample strongly differs from the behavior of the co-implanted ones. While B diffuses very deeply when implanted alone, in co-implanted samples, both N + B and N + C + B, diffusion is strongly retained. Two phenomena may be responsible for this slowing-down of the diffusion, one occurring at the near-surface region, where the B concentration is comparable to the Si one, and the other in the underlying regions, where B is of the order of or below the solubility limit. Near the surface region the formation of BN or BCN stable clusters may reduce the available diffusion source. Additionally, the appearance of SiC clusters may contribute to decrease the effective surface of the diffusion source. In deeper regions, trapping of Si self-interstitials by carbon [23, 24], and even by N [31], atoms is responsible for the slowing-down of the transient enhanced diffusion of boron.

Because of the high-temperature annealing processes, it is expected that most of the F atoms out-diffuse [32], leaving a high density of extended end-of-range (EOR) defects that also prevents excessive transient enhanced diffusion [33, 34]. This effect is especially apparent in B-only-implanted samples. The diffusion depth after RTA in this sample is lower than in the N + B or the N + C + B ones, while the opposite occurs after furnace annealing; however, a large damage remains in the B-only-implanted samples. In these samples the FWHM of the main (111) peak is considerably wider than in N + B and N + C + B samples (see Figs. 3, 4, and 5). A large disorder remains in the surface layer of the B-implanted sample, even after the 1200 °C furnace annealing (see Fig. 3), whereas the presence of N and N + C helps considerably to the damage recovery.

The annealing behavior of N + B- and N + C + B-implanted samples is also different. In the N + B samples three layers are clearly distinguished by TEM (see Fig. 8), a polycrystalline silicon layer with α and β-Si_3N_4 inclusions at the surface, followed by an amorphous layer and a highly defective Si layer, also with silicon nitride clusters. Because of the high doping, the surface polycrystalline layer exhibits a strong light absorption and, thus, ellipsometry is sensitive only to the most external part. In fact, the fitting of the SE spectra requires the use of strongly doped silicon (SiB21) and shows that this layer is not homogeneous and needs the use of a nearly transparent material, like amorphous or h-BN, as a database, in a deeper layer to get a reasonable fitting.

On the contrary, TEM images of the N + C + B-implanted samples show a structure of two layers, being polycrystalline silicon layer with clusters, followed by an amorphous layer. This structure is confirmed by SE measurements but, even in this case, the most external layers must be inhomogeneous because of the need of deeper layers with more transparent material like h-BN or SiC.

5 Conclusions

TEM studies show that, after annealing, the N + B-implanted samples exhibit near the surface a three-layer structure, whereas in those implanted with N + C + B there are only two layers clearly distinguished. In the N + B-implanted sample the intermediate layer (2) is amorphous, the outer layer (1) is a mixture of amorphous and crystalline phases, and the inner layer (3) is highly defective crystalline silicon with inclusions of other phases.

Ellipsometry is sensitive just to a part of the most external of the layers seen by TEM. In the RTA annealed samples, both N + B and N + C + B co-implanted ones, ellipsometry suggests the majority presence of a BN phase in the external layer that could be fitted using the dielectric constant of hexagonal boron nitride. This is in accordance with the BN vibrational mode detected by IR, associated with the h-BN phase. However, since it has not been detected by SAED, we believe that boron nitride could be amorphous because the IR vibrational mode and the dielectric constant of amorphous and hexagonal BN could be very similar.

After the three-hour annealing at 1200 °C, the fraction of amorphous material in the outer layer decreases, becoming mainly highly ordered polycrystalline silicon, with some inclusions of α- and β-Si_3N_4. These phases were also detected in layer 3.

XRD results show that co-implantation of N + B and N + C + B helps in the damage recovery as compared to samples implanted with boron only. Furthermore, the additional implantation of N and C prevents the excessive diffusivity of B. The implanted samples exhibit, after high-temperature annealing, a lattice-parameter reduction between 0.7 and 1.0%. This reduction is mainly due to B substitutionals.

All the results point to a more stable structure of the N + C + B-implanted layer than the N + B ones, that opens the possibility to BCN buried layers in silicon.

ACKNOWLEDGEMENTS This work has been financed by Project Nos. MAT98-0823-C03-02/03 and MAT2000-0478-P4-02 and the Junta de Andalucía (Group Tep-0120). TEM measurements were carried out at the 'División de Microscopí a Electrónica, SCCYT, Universidad de Cádiz'. One of the authors, F.M. Morales, would like to thank G. Aragón for economic support and F. León for the collaboration in TEM sample preparation. L. Barbadillo is grateful for the support of the Comunidad de Madrid under an FPI grant. We also thank C.J. Pastor for his technical assistance in the XRD measurements.

REFERENCES

1 R.H. Wentorf, Jr.: J. Chem. Phys. **36**, 1990 (1962)
2 A.Y. Liu, M.L. Cohen: Science **245**, 8419 (1989)
3 M.L. Cohen: Phys. Rev. B **32**, 7988 (1985)
4 A.Y. Liu, M.L. Cohen: Phys. Rev. B **41**, 107 27 (1990)
5 N.J. Pipkin: J. Mater. Sci. **15**, 2651 (1980)
6 O. Mishima, K. Era, J. Tanaka, S. Yamaoka: Appl. Phys. Lett. **53**, 962 (1988)
7 C.A. Taylor, II, S.W. Brown, V. Subramaniam, S. Kidner, S.C. Rand, R. Clarke: Appl. Phys. Lett. **65**, 1251 (1994)
8 D.J. Kester, R. Messier: J. Appl. Phys. **72**, 504 (1992)
9 M. Gasgnier, H. Szwarc, A. Ronez: J. Mater. Sci. **35**, 3003 (2000)
10 H.-G. Boyen, P. Widmayer, D. Schwertberger, N. Deyneka, P. Ziemann: Appl. Phys. Lett. **76**, 709 (2000)
11 H. Saitoh, W.A. Yarbrough: Appl. Phys. Lett. **58**, 2228 (1991)
12 L. Jiang, A.G. Fitzgerald, M.J. Rose, A. Lousa, S. Gimeno: Appl. Surf. Sci. **167**, 89 (2000)
13 M.O. Watanabe, S. Itoh, T. Sasaki, K. Mizushima: Phys. Rev. Lett. **77**, 187 (1996)
14 M.O. Watanabe, S. Itoh, K. Mizushima, T. Sasaki: J. Appl. Phys. **78**, 2880 (1995)
15 J. Yu, E.G. Wang, J. Ahn, S.F. Yoon, Q. Zhang, J. Cui, M.B. Yu: J. Appl. Phys. **87**, 4022 (2000)
16 X.D. Bai, E.G. Wang, J. Yu, H. Yang: Appl. Phys. Lett. **77**, 67 (2000)
17 J.F. Ziegler: *SRIM Program* (IBM Research, Yorktown Heights, NY 1996)
18 A.C. Adams: Solid State Technol. **26**, 135 (1983)
19 G. Spitzer, D.A. Kleiman, D. Walsh: Phys. Rev. **113**, 127 (1959)
20 R. Geick, C.H. Perry, G. Rupprecht: Phys. Rev. **146**, 543 (1966)
21 P.J. Gielisse, S.S. Mitra, J.N. Plendl, R.D. Griffis, L.C. Mansur, R. Marshall, E.A. Pascoe: Phys. Rev. **155**, 1039 (1967)
22 S. Isomae, T. Ishiba, T. Ando, M. Tamura: J. Appl. Phys. **74**, 3815 (1993)
23 H. Rücker, B. Heineman, W. Röpke, R. Kurps, D. Krüger, G. Lippert, H.J. Osten: Appl. Phys. Lett. **73**, 1682 (1998)
24 R. Scholz, U. Gösele, J.-Y. Huh, T.Y. Tan: Appl. Phys. Lett. **72**, 200 (1998)
25 R.M. Azzam, N.M. Bashara: *Ellipsometry and Polarized Light* (North-Holland, Amsterdam 1987)
26 D.E. Aspnes, J.B. Theeten: J. Appl. Phys. **50**, 4928 (1979)
27 W.J. Choyke, E.D. Palik: *Handbook of Optical Constants of Solids*, ed. by E.D. Palik (Academic, New York 1985) p. 587
28 H.G. Tompkins: *A User's Guide to Ellipsometry* (Academic, New York 1993) p. 246
29 D.M. Hoffman, G.L. Doll, P.C. Eklund: Phys. Rev. B **30**, 6051 (1984)
30 L. Viña, M. Cardona: Phys. Rev. B **29**, 6739 (1984)
31 M. Herden, A.J. Bauer, M. Beichele, H. Ryssel: Solid State Electron. **45**, 1251 (2001)
32 M. Tamura, Y. Hiroyama, A. Nishida: Mater. Chem. Phys. **54**, 23 (1998)
33 M.Y. Tsai, D.S. Day, B.G. Streetman, P. Williams, C.A. Evans, Jr.: J. Appl. Phys. **50**, 188 (1979)
34 A. Dusch, J. Marcon, K. Masmoudi, F. Olivié, M. Benzohra, K. Ketata, M. Ketata: Mater. Sci. Eng. B **80**, 65 (2001)